Liquid Water Visualization in the Pt-Loading Catalyst Layers of Polymer Electrolyte Fuel Cells Using *Operando* Synchrotron X-ray Radiography

Wataru Yoshimune, Akihiko Kato, Tetsuichiro Hayakawa, Satoshi Yamaguchi, and Satoru Kato*

W. Yoshimune, A. Kato, T. Hayakawa, S. Yamaguchi, S. Kato
Toyota Central R&D Labs, Inc.
Nagakute, Aichi 480-1192, Japan
E-mail: yoshimune@mosk.tytlabs.co.jp

Keywords: X-ray radiography, liquid water, catalyst layer, polymer electrolyte fuel cell, water management

Water management is important for addressing the challenges posed by next-generation fuel cell electric vehicles. Although X-ray imaging techniques are useful for probing the mechanism of water transport in the gas diffusion layer of polymer electrolyte fuel cells, they cannot be easily applied to the Pt-loading catalyst layer because of its low X-ray transmittance due to the high absorption coefficient of Pt. Herein, we propose a method to realize the high-resolution X-ray imaging of the cathode catalyst layer in polymer electrolyte fuel cells using synchrotron X-ray radiography, thus bridging the above gap. The results of *operando* synchrotron X-ray radiography measurements reveal that water accumulation in the cathode catalyst layer depends on the cell temperature, feed gas humidity, and cell voltage, while time-slice analysis shows that the water accumulation rate in the cathode catalyst layer is approximately four times that in the cathode gas diffusion layer. The proposed imaging method can be used to evaluate the water uptake capability of the catalyst layer and thus deepen our understanding of flooding phenomena and cold-start behavior at subzero temperatures.

1. Introduction

The unique properties of water, e.g., its high specific heat capacity, vapor pressure, and relative dielectric constant, are important for numerous applications. The sorption of water vapor by porous media is essential for water-harvesting devices and water-source heat pumps.[1] The evaporation of liquid water plays a pivotal role in food processing, chemical purification, battery-electrode drying, and other industrial processes.[2] Moreover, water circulation through fuel cells and electrolyzers is important for realizing a hydrogen-based society.[3]

The nondestructive visualization of liquid water using synchrotron X-ray and neutron analyses facilitates progress in the above fields.[4] The extent of the interaction between X-rays and electron clouds is positively correlated with the atomic number (*Z*-number), whereas the strength of the interaction between neutrons and nuclei is not correlated with the *Z*-number and is nucleus-specific. Compared with X-ray analysis, neutron analysis is more liquid-water-sensitive and can detect even small differences in liquid-water content. For example, *in situ* small-angle neutron scattering has been used to examine water evaporation in porous media,[5] neutron radiography has provided insights into the water distribution in polymer electrolyte fuel cells (PEFCs) covered with metal endplates,[6] and neutron analysis has enabled the study of water dynamics[7] and water/ice identification.[8] However, neutron analysis generally exhibits lower spatial and temporal resolution than X-ray analysis, and liquid-water visualization in microstructures is therefore often performed using synchrotron X-ray characterization techniques, including radiography,[9] tomography,[10] small-angle scattering,[11] and Compton scattering.[12] Subsecond X-ray tomography has been used to probe water evaporation in catalysts[10d] and water dynamics in PEFCs,[10e] while *operando* X-ray Compton scattering has been used to visualize water distribution in PEFCs.[12b] Despite the advances in these three-dimensional characterization techniques, two-dimensional X-ray radiography remains a simple yet powerful tool for liquid-water visualization.

In PEFCs, protons produced from hydrogen gas in the anode catalyst layer (CL) pass through a proton exchange membrane (PEM) to reach the Pt surface at the cathode CL, where they react with oxygen to generate electricity and heat.[13] Water produced as a byproduct of the oxygen reduction reaction at the cathode CL must be effectively removed into the flow-field (FF) plate through the gas diffusion layer (GDL). During operation at low temperatures (i.e., those below the water condensation point), the liquid water accumulated in the cathode CL hinders the delivery of oxygen to the Pt surface.[14] Conversely, PEMs exhibit proton conductivity only when adequately hydrated.[15] Therefore, water content and distribution control, particularly in the cathode CL, is crucial for realizing optimal PEFC performance.[16] However, most *operando*

studies have focused on the distribution of water in PEMs, GDLs, and FF plates but have not targeted the cathode CL because of the high X-ray absorption capacity of Pt and the thickness fluctuation of hydrated PEMs.[10g] The above challenges can be overcome using Pt-group metal (PGM)-free CLs with thicknesses of ~100 μm. X-ray radiography and tomography have been used to propose a water-transport mechanism and proper water-management strategy for PGM-free CLs in PEFCs.[17] Information on the distribution of water in conventional Pt-loading and PGM-free CLs as well as PGM-free CLs is useful for the development of next-generation fuel cell electric vehicles (FCEVs).

To bridge the above gap, we herein developed an *operando* cell to visualize the distribution of liquid water in the Pt-loading cathode CL of a PEFC using synchrotron X-ray radiography, probed the effects of cell temperature, feed gas humidity, and cell voltage on this distribution, and examined the transient liquid-water accumulation behavior in the cathode CL.

2. Results and Discussion

2.1. Cell Design Based on Theoretical Principles

The X-ray transmittance of the *operando* cell used for liquid-water visualization by X-ray absorption contrast imaging should be sufficient for distinguishing between dry and wet states. The absorption-based attenuation of X-rays is described by the Beer–Lambert law:

$$\frac{I}{I_0} = e^{-\mu l}, \tag{1}$$

where I_0 and I are the intensities of the incident and transmitted X-rays, respectively, μ is the X-ray energy–dependent attenuation coefficient of the medium, and l is the thickness of the medium in the X-ray propagation direction. The X-ray irradiation of PEFC components for liquid-water visualization is usually performed at energies of 10–20 keV to avoid the damage caused by low-energy (<10 keV) irradiation and ensure a sufficient contrast difference between these components and liquid water above 20 keV.[18] Roth et al.[18b] ascribed ionomer decomposition in Pt-containing CLs to the emission of secondary electrons from the irradiated Pt. Therefore, in our previous studies,[9d–g] the energy of the incident X-rays was set to 11.4 keV (below the Pt L_3 edge) to avoid their absorption by Pt, and the irradiation intensity was attenuated to 10% of the original to reduce damage. **Figure 1** shows X-ray transmittance at 11.4 keV as a function of X-ray path length for different Pt-loading CLs with an ionomer/carbon mass ratio (I/C) of 0.75. The X-ray transmittances of dry CLs were calculated using the volume fractions of Pt, carbon, Nafion ionomer, and pores (**Table 1**).

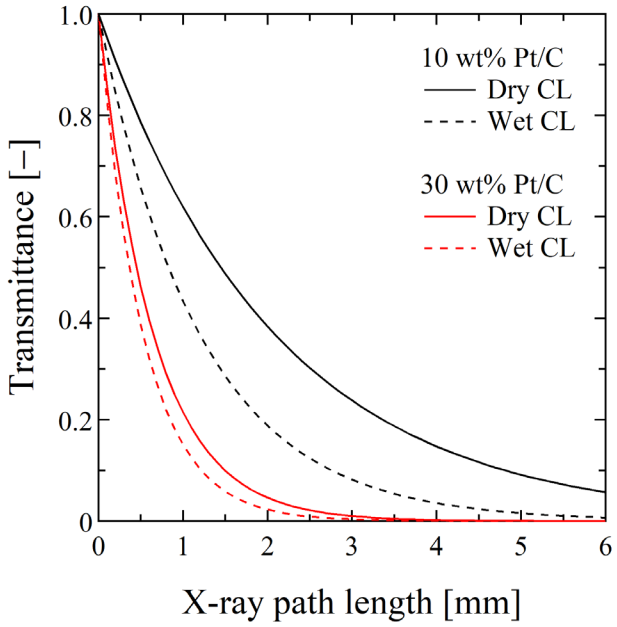

Figure 1. Calculated X-ray transmittances of dry and wet catalyst layers (CLs) at 11.4 keV.

Table 1. Compositions of Pt-loading CLs used for X-ray transmittance calculations.

CL	Pt [vol%]	Carbon [vol%]	Ionomer [vol%]	Pore [vol%]
TEC10V10E I/C = 0.75	0.2[a)]	22.7[a)]	17.1[a)]	60[b)]
TEC10V30E I/C = 0.75	0.9[a)]	22.3[a)]	16.8[a)]	60[b)]

[a)]Calculated from the composition of the catalyst ink. [b)]Reference value reported elsewhere.[19]

Wet CLs were defined as those with pores completely filled with liquid water. The theoretical μ values of Pt (1613.52 cm^{-1}), carbon (2.57 cm^{-1}), Nafion ionomer (11.38 cm^{-1}), and water (3.44 cm^{-1}) at 11.4 keV were used.[20] According to these calculations, in an *operando* cell with an X-ray path length of 6 mm,[9d–g] the transmitted X-rays are attenuated to <0.01% by typical CLs (30 wt% Pt on Vulcan XC-72 carbon; Pt/C), and no discrimination between the dry and wet states is possible. The theoretical attenuation curves suggested that X-ray path length is negatively correlated with X-ray transmittance and indicated that an *operando* cell with an X-ray path length of ≤2 mm should provide a transmittance difference (~1.1%) sufficient for visualizing liquid water in CLs (30 wt% Pt/C). Alternatively, one can reduce the volume fraction of Pt in CLs.[10g] In the case of a low-Pt-loading CL (10 wt% Pt/C), the *operando* cell with an X-ray path length of 6 mm was found to exhibit a transmittance difference (~1.5%) sufficient for water-content quantitation. Herein, *operando* cells with different X-ray path

lengths but the same Pt thickness in the X-ray propagation direction were prepared to visualize liquid water in the cathode CL. The coating area and thickness of catalyst-coated membranes (CCMs) were controlled using a spraying method (Figure S1a).[21] The *I–V* performance of CCMs fabricated using the spraying method was inferior to that of CCMs transferred by the decal method (Figure S2),[22] which is commonly used in the production of FCEVs. Nevertheless, the spraying method was selected because of its suitability for the fabrication of CLs of arbitrary uniform thickness without cracks in a defined area (Figure S1b).

2.2. *Operando* Measurement Setup

Figure 2a illustrates the setup used for *operando* X-ray radiographic measurements (X-ray propagation direction = *z*-direction). The *operando* cell, designed to prevent X-ray attenuation by current collectors, was placed in the X-ray path and maintained at the desired temperature using cartridge heaters inserted into metal end plates. Figure 2b shows the internal structure of the *operando* cell and the region imaged to observe the cross-sectional water distribution (666 µm × 666 µm). A minimum pixel size of 0.325 µm was achieved without the use of Fresnel zone plates or similar X-ray imaging optical systems.

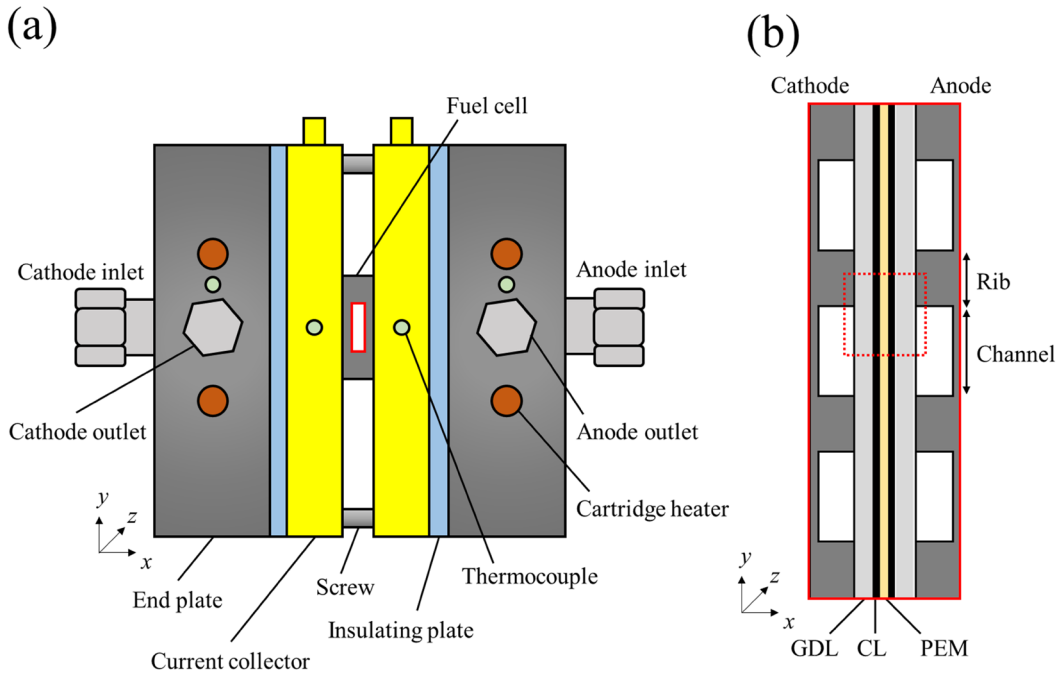

Figure 2. a) Setup used for *operando* X-ray radiographic measurements, with the actual cell represented by a red solid line–enclosed rectangle. b) Close-up configuration of the *operando* cell, with the red dotted line–enclosed square corresponding to the imaging area. GDL = gas diffusion layer, PEM = proton exchange membrane.

Figure S3 shows liquid-water distributions in *operando* cells with X-ray path lengths of 2 and 6 mm obtained at a cell temperature of 40 °C, relative humidity (RH) of 80%, and cell voltage of 0.2 V. The blurred image obtained at an X-ray path length of 6 mm was ascribed to the nonuniformity of the liquid-water distribution, material/pore morphology, and sample orientation/distortion in the direction of X-ray propagation and the fact that radiographic measurements provide integrated two-dimensional information. These adverse effects can be mitigated by shortening the X-ray path length for *operando* radiographic measurements (Figure S3). In the following section, we present data obtained using an X-ray path length of 2 mm, which corresponds to an effective CCM area of 0.08 cm^2.

The cell was designed to prevent gas leakage and ensure the visualization of water at the cathode CL (Figure S4). The *I–V* performance was sufficient for liquid-water visualization (Figure S5). The cathode CL had a thickness of ~30 μm and porosity of ~0.7 (Figure S6). High-resolution X-ray imaging indicated that the position drift of the cell body during *operando* measurements was ±1 μm (Figure S7) and did not depend on cell temperature (Table S1). Changes in X-ray attenuation (Figure S8) indicated that the PEM swelled by ~0.3 μm during power generation (Figure S9). The observed water content did not match that calculated from the total current because of the limited field of view. Given that a suitable transmittance difference could not be achieved without a large amount of liquid water, high current densities were realized for a small CCM area (Table S2). Moreover, the material balance of the water supplied by the humidified feed gas was considered (Figure S10).

2.3. Water Distribution in Cathode CL

2.3.1. Segmentation of PEFC Components

Figure 3 shows a representative liquid-water distribution in the *operando* cell. The substrate, microporous layer (MPL), MPL/CL interface, and CL regions were segmented based on the dry-state transmittance of the under-rib and channel regions (Figure S6a and S6b). The brightness of the substrate region was nonuniform because of the nonuniformity of carbon-fiber and polytetrafluoroethylene distribution. A gradient decrease in brightness upon moving from the substrate to the MPL region was observed. In GDLs, MPLs are formed in the substrate macropores. The intrusion region was not defined, as it was beyond the scope of this study, and was divided into substrate and MPL regions at the brightness midpoint between the substrate and MPL. The abrupt decrease in brightness upon moving from the MPL to the CL region corresponded to the MPL/CL interface region. The CL had a thickness of ~30 μm, and the PEM

had the lowest brightness. The porosity of the spray-coated CL was estimated as ~0.7 (0.6 for typical CLs) from the X-ray transmittances of the CL and PEM regions (Figure S6c).

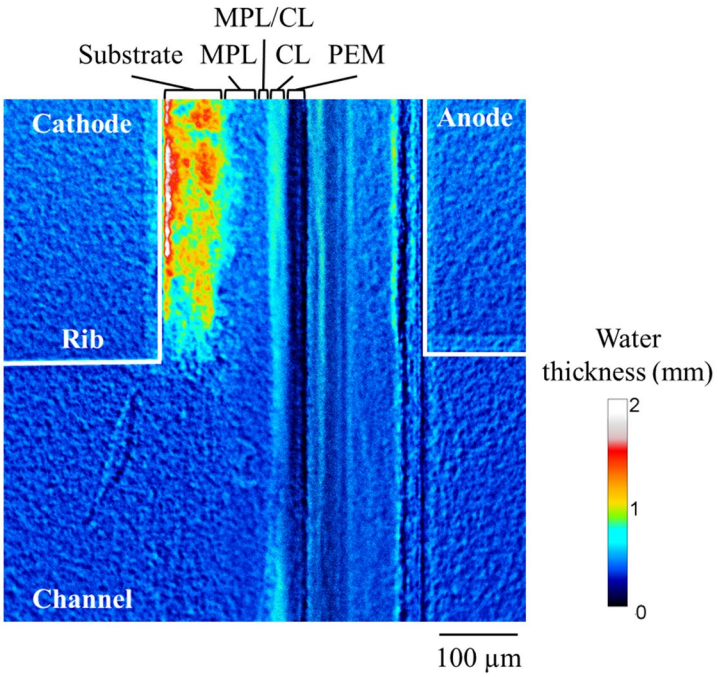

Figure 3. Liquid-water distribution in the *operando* cell 600 s after the start of power generation at 40 °C and 80% RH. MPL = microporous layer.

2.3.2. Effect of Operation Conditions

Operando measurements were performed at 40, 50, and 60 °C and various RHs. Little liquid water was observed at 60 °C. Shum et al.[23] pointed out that at operating temperatures above 50 °C, the produced water is eliminated via the manifold as water vapor. Therefore, a detailed analysis was performed using the data obtained at 40 and 50 °C. **Figure 4** shows that at 40 °C and 80% RH, the thickness of the water layer was close to zero at a cell voltage of 0.6 V and increased with decreasing voltage. Liquid water tended to accumulate under the rib at the CL and MPL/CL interfaces rather than in the channel, which has not been quantitatively demonstrated before. Notably, the water thickness in the former locations saturated at a cell voltage of 0.4 V. Conversely, the water thickness in the GDL under the rib linearly increased up to a cell voltage of 0.2 V. The accumulation of water at the MPL/CL interface causes flooding and thus considerably deteriorates *I–V* performance.[24] Although liquid water accumulated at the interface, its content was lower than that in the CL. The liquid water accumulating at the interface was rapidly discharged through cracks and pores in the MPL (Movie S1), which resulted in a low liquid-water content therein.

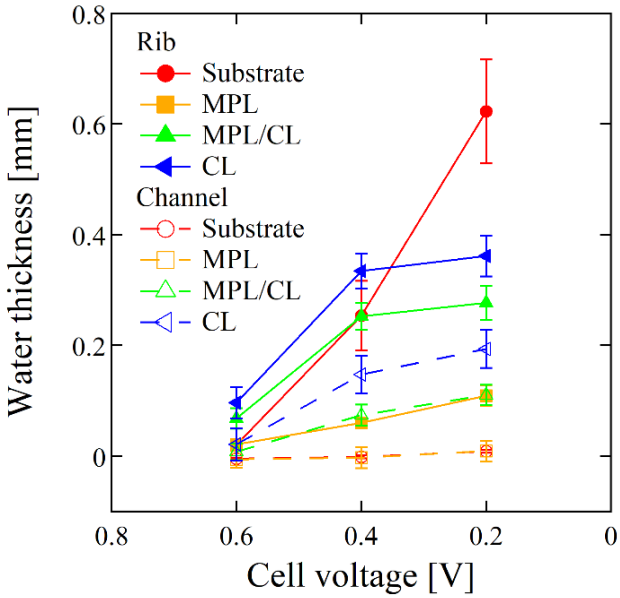

Figure 4. Liquid-water thickness in polymer electrolyte fuel cell cathode components as a function of cell voltage.

The effects of RH and cell temperature on water thickness are summarized in Figure S11. *Operando* experiments conducted at RHs of up to 120% revealed the dominant influence of the amount of condensed water derived from the wet feed gas (Figure S10b); therefore, the influence of the produced water could not be discussed. The water thickness at 80% RH was smaller than that at 100% RH (Figure S11a), which was related to the lower power generation in the latter case (Table S2 and Figure S10a). In contrast, a characteristic trend was observed for cell temperature (Figure S10b). The water thickness decreased with increasing cell temperature, and the extent of this decrease followed the order of substrate < MPL < MPL/CL < CL. This behavior indicated that the water-thickness decrease was the largest in the region closer to the power-generation section at higher cell temperatures, which was explained by the temperature gradient established in the PEFC components during power generation.[25]

2.3.3. Transient Liquid-Water Behavior

The transient behavior of the liquid-water distribution under the rib was examined at a cell voltage of 0.2 V, temperature of 40 °C, and RH of 80%. **Figure 5** shows time-sliced transmittance profiles. During *operando* measurements, the transmittance was closest to unity immediately after the onset of power generation, decreasing in the following 200 s and then stabilizing. A decrease in transmittance corresponds to an increase in the amount of accumulated water. The substrate transmittance decreased slower than the CL transmittance. Binning was performed in each region, and the resulting transmittance was converted to water

thickness for the further analysis of water content immediately after the start (**Figure 6**a). The water thickness in each region except the substrate increased with time, with an inflection point corresponding to a drop in the rate of this increase observed at ~10 s. Figure 6b shows the water accumulation rate (defined as the rate of the water-thickness increase) obtained by fitting the water thickness–time plot in the region between zero and ~10 s (inflection point) to a straight line. The order of the water accumulation rate showed that the produced water first accumulated in the CL and subsequently drained through the MPL and accumulated in the GDL. It was found that the water accumulation rate in the CL was about four times that in the GDL.

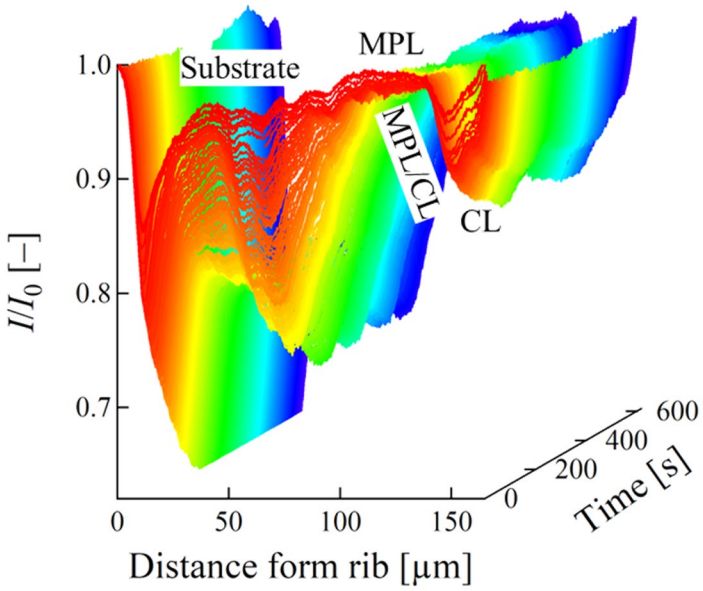

Figure 5. Waterfall plot of transmittance change at the cathode under the rib during operando measurement at a cell voltage of 0.2 V, temperature of 40 °C, and relative humidity of 80%.

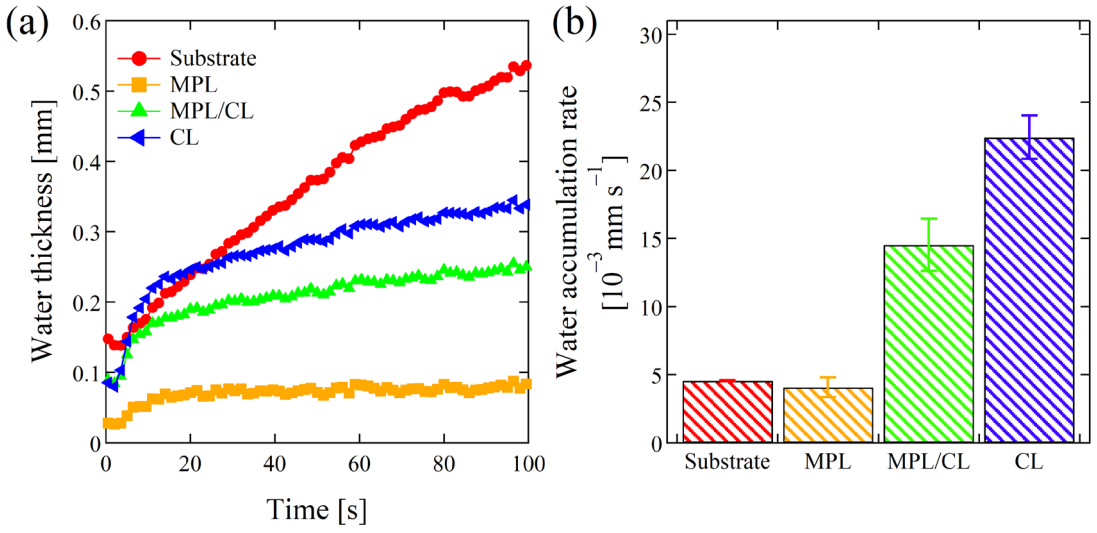

Figure 6. (a) Temporal dependence of water thickness under the rib after the start of power generation. (b) Water accumulation rate immediately after the power generation onset.

3. Conclusion

The difficulty in visualizing liquid water in the Pt-loaded CLs of PEFCs due to the strong absorption of X-rays by Pt was rationalized by X-ray transmittance calculations and addressed by fabricating an operando cell with a reduced CL thickness in the X-ray propagation direction. Operando synchrotron X-ray radiography enabled the visualization of liquid water in the Pt-loaded CL of this cell, namely the quantitation of the liquid-water volume and its transient changes in different regions (GDL, MPL, MPL/CL interface, and CL). Liquid-water accumulation at the MPL/CL interface and in the CL was found to occur under the rib and on the substrate. Time-slice analysis demonstrated that the water accumulation order was CL → MPL/CL interface → substrate. The developed approach provides information on the liquid-water saturation level in CLs, which is typically assumed for flooding simulation studies on PEFC performance,[26] and can be used to examine the validity of the concept of the water-uptake properties of the cathode CL, which is used as an indicator of cold-start capability at subzero temperatures.[27]

4. Experimental Section

Materials: Pt nanoparticles supported by Vulcan carbon (TEC10V10E, 9.7 wt% Pt; TEC10V30E, 29.3 wt% Pt; Tanaka Kikinzoku Kogyo), the Nafion dispersion (D2020CS, Chemours) and membrane (NR211, Chemours), and the GDL (22BB, SGL Carbon) were used as received. Ethanol (99.5%) was purchased from FUJIFILM Wako Pure Chemicals. Ultrapure water (resistivity > 18.2 MΩ cm, total organic carbon < 5 ppb) produced using a Milli-Q system (Millipore) was used for catalyst-ink formulation.

Sample Preparation: Pt/C (TEC10V10E or TEC10V30E, 300 mg) and the Nafion ionomer (988 or 767 mg) were dispersed in ethanol:deionized water (3:1, v/v; 47.7 or 43.5 mL) to afford catalyst inks with a solid content of 1.0 wt% and an I/C of 0.75. A glass vial containing the ink was placed in an ultrasonic bath filled with cold water (<5 °C) and sonicated for 10 min to break down carbon agglomerates.[28] The catalyst ink was supplied to an ultrasonic atomizer (spray nozzle: NS130K50, spray shaper: WVSAS, SONAER) using a syringe driver (YSP-201, YMC) and sprayed onto the surface of the Nafion membrane. The detailed setup for spray-coating has been described elsewhere.[19] The ink and nitrogen supply rates were 100 μL min^{-1} and 1 L min^{-1}, respectively. The distance between the nozzle and membrane was 8 cm. These parameters and the composition of the catalyst ink were optimized to avoid the formation of a slushy layer on the membrane. The spraying duration required to obtain a film thickness of 30 μm was selected based on the corresponding calibration curve (Figure S1). After spraying one

side of the membrane, we sprayed the opposite side to obtain a film thickness of 10 μm for the anode. The CCM area was defined as a 2.0 mm × 4.0 mm rectangle using an in-house-made mask.

Operando X-ray Radiography: The operando cell was assembled by sandwiching the CCM between GDLs with ethylene propylene diene monomer gaskets (100 μm) and then between in-house separators made of a resin-impregnated graphite block and featuring three gas channels (G347B, Tokai Carbon).[9d] The 30 μm–thick CL of the CCM was used as the cathode. Operando synchrotron X-ray radiography experiments were conducted at an X-ray energy of 11.4 keV using the BL33XU beamline at the SPring-8 facility.[29] The transmitted X-rays were detected using an X-ray CMOS camera (ORCA-Flash 4.0 sCMOS sensor, Hamamatsu Photonics). The resolution of each pixel was 0.325 μm, and the field of view was 665.6 μm × 665.6 μm. The exposure time was 1 s (interval = 0.5 s). The cell potential was controlled using a potentiostat (HZ-7000, Hokuto Denko), and high-frequency (10 kHz) resistance was measured using a resistance meter (356E, Tsuruga Denki). The flow rates of the supplied gases were controlled using mass-flow controllers (FCST1000ML, Fujikin), and temperature-controlled bubblers were used for gas humidification. The cell potential, current density, high-frequency resistance, and transmitted X-ray images were recorded simultaneously. The images were acquired at 40 °C, with synthetic air (300 cm^3 min^{-1}) supplied to the cathode and hydrogen (200 cm^3 min^{-1}) supplied to the anode. The steady-state current at four potential steps (open-circuit voltage (OCV) and 0.6, 0.4, and 0.2 V) was measured while holding each potential for 10 min. The transmittance images were recorded while the cell voltage was held constant. After a series of chronoamperometric measurements, the RH of the feed gases supplied to both electrodes was sequentially increased to 80%, 100%, and 120%. The amount of water in the channel direction, represented by the equivalent water thickness (t_{water}), was quantified using the Beer–Lambert law:

$$t_{\mathrm{water}} = \frac{1}{\mu} \ln \frac{T_{\mathrm{dry}}}{T}, \tag{2}$$

where μ is the attenuation coefficient for water (0.344 mm^{-1} at an X-ray energy of 11.4 keV[20]), T_{dry} is the intensity of transmitted X-rays in the absence of liquid water (at the OCV), and T is the intensity of transmitted X-rays during power generation.

Supporting Information

Supporting Information is available from the Wiley Online Library or from the author.

Acknowledgements

Synchrotron radiation experiments were performed at the BL33XU beamline of SPring-8 with the approval of JASRI (proposal nos. 2023A7032, 2023B7032, and 2024A7032).

Conflict of Interest

The authors declare no conflict of interest.

Author Contributions

W.Y. and S.K. conceived the study and designed experiments. W.Y. and A.K. prepared the samples. W.Y. performed electrochemical characterization. W.Y., A.K., T.H., S.Y., and S.K. performed synchrotron X-ray experiments. W.Y. analyzed the X-ray images obtained for water visualization. W.Y. wrote the first draft of the manuscript. All authors discussed the results and approved the final version of the manuscript.

Data Availability Statement

Data supporting the findings of this study are available from the corresponding author upon request.

Received: ((will be filled in by the editorial staff))
Revised: ((will be filled in by the editorial staff))
Published online: ((will be filled in by the editorial staff))

References

[1] a) Y. Tu, R. Wang, Y. Zhang, J. Wang, *Joule* **2018**, *2*, 1452; b) H. Lu, W. Shi, Y. Guo, W. Guan, C. Lei, G. Yu, *Adv. Mater.* **2022**, *34*, 2110079; c) M. F. de Lange, K. J. F. M. Verouden, T. J. H. Vlugt, J. Gascon, F. Kapteijn, *Chem. Rev.* **2015**, *115*, 12205.

[2] Y. S. Zhang, N. E. Courtier, Z. Zhang, K. Liu, J. J. Bailey, A. M. Boyce, G. Richardson, P. R. Shearing, E. Kendrick, D. J. L. Brett, *Adv. Energy Mater.* **2022**, *12*, 2102233.

[3] Y. Wang, Y. Pang, H. Xu, A. Martinez, K. S. Chen, *Energy Environ. Sci.* **2022**, *15*, 2288.

[4] W. Yoshimune, *Bull. Chem. Soc. Jpn.* ***inpress***. DOI: 10.1093/bulcsj/uoae046

[5] W. Yoshimune, S. Kato, M. Harada, *ACS Appl. Mater. Interfaces* **2022**, *14*, 17396.

[6] a) J. P. Owejan, T. A. Trabold, D. L. Jacobson, D. R. Baker, D. S. Hussey, M. Arif, *Int. J. Heat Mass Transfer* **2006**, *49*, 4721; b) C. Hartnig, I. Manke, R. Kuhn, N. Kardjilov, J. Banhart, W. Lehnert, *Appl. Phys. Lett.* **2008**, *92*, 134106; c) J. M. LaManna, S. Chakraborty, J.

J. Gagliardo, M. M. Mench, *Int. J. Hydrogen Energy* **2014**, *39*, 3387; d) N. J. Cooper, A. D. Santamaria, M. K. Becton, J. W. Park, *Int. J. Hydrogen Energy* **2017**, *42*, 16269; e) A. Mohseninia, D. Kartouzian, R. Schlumberger, H. Markötter, F. Wilhelm, J. Scholta, I. Manke, *ChemSusChem* **2020**, *13*, 2931; f) J. Lee, S. Escribano, F. Micoud, G. Gebel, S. Lyonnard, L. Porcar, N. Martinez, A. Morin, *ACS Appl. Energy Mater.* **2020**, *3*, 8393; g) M. Nasu, H. Yanai, N. Hirayama, H. Adachi, Y. Kakizawa, Y. Shirase, H. Nishiyama, T. Kawamoto, J. Inukai, T. Shinohara, H. Hayashida, M. Watanabe, *J. Power Sources* **2022**, *530*, 231251; h) W. Yoshimune, Y. Higuchi, A. Kato, S. Hibi, S. Yamaguchi, Y. Matsumoto, H. Hayashida, H. Nozaki, T. Shinohara, S. Kato, *ACS Energy Lett.* **2023**, *8*, 3485.

[7] a) J. Perrin, C. Lyonnard, S. Volino, *J. Phys. Chem. C* **2007**, *111*, 3393; b) O.-E. Haas, J. M. Simon, S. Kjelstrup, A. L. Ramstad, P. Fouquet, *J. Phys. Chem. C* **2008**, *112*, 3121; c) K. Ito, T. Yamada, A. Shinohara, S. Takata, Y. Kawakita, *J. Phys. Chem. C* **2021**, *125*, 21645.

[8] a) J. Biesdorf, P. Oberholzer, F. Bernauer, A. Kaestner, P. Vontobel, E. H. Lehmann, T. J. Schmidt, P. Boillat, *Phys. Rev. Lett.* **2014**, *112*, 248301; b) M. Siegwart, F. Huang, M. Cochet, T. J. Schmidt, J. Zhang, P. Boillat, *J. Electrochem. Soc.* **2020**, *167*, 064510; c) Y. Higuchi, D. Setoyama, K. Isegawa, Y. Tsuchikawa, Y. Matsumoto, J. D. Parker, T. Shinohara, Y. Nagai, *Phys. Chem. Chem. Phys.* **2021**, *23*, 1062; d) K. Isegawa, D. Setoyama, Y. Higuchi, Y. Matsumoto, Y. Nagai, T. Shinohara, *Nucl. Instrum. Methods Phys. Res., Sect. A* **2022**, *1040*, 167260; e) Y. Higuchi, W. Yoshimune, S. Kato, S. Hibi, D. Setoyama, K. Isegawa, Y. Matsumoto, H. Hayashida, H. Nozaki, M. Harada, N. Fukaya, T. Suzuki, T. Shinohara, Y. Nagai, *Commun. Eng.* **2024**, *3*, 33.

[9] a) T. Sasabe, P. Deevanhxay, S. Tsushima, S. Hirai, *Electrochem. Commun.* **2011**, *13*, 638; b) R. Alink, J. Haußmann, H. Markötter, M. Schwager, I. Manke, D. Gerteisen, *J. Power Sources* **2013**, *233*, 358; c) J. Haußmann, H. Markötter, R. Alink, A. Bauder, K. Dittmann, I. Manke, J. Scholta, *J. Power Sources* **2013**, *239*, 611; d) A. Kato, S. Kato, S. Yamaguchi, T. Suzuki, Y. Nagai, *J. Power Sources* **2022**, *521*, 230951; e) T. Suzuki, A. Kato, S. Yamaguchi, Y. Nagai, D. Hayashi, S. Kato, *J. Power Sources Adv.* **2023**, *22*, 100119; f) M. Inagaki, A. Kato, S. Kato, T. Suzuki, S. Yamaguchi, *Int. J. Hydrogen Energy* **2024**, *58*, 14; g) A. Kato, S. Kato, S. Yamaguchi, T. Suzuki, Y. Nagai, *Int. J. Hydrogen Energy* **2024**, *50*, 1218.

[10] a) J. Eller, J. Roth, F. Marone, M. Stampanoni, F. N. Büchi, *J. Electrochem. Soc.* **2017**, *164*, F115; b) Y. Nagai, J. Eller, T. Hatanaka, S. Yamaguchi, S. Kato, A. Kato, F. Marone, H. Xu, F. N. Büchi, *J. Power Sources* **2019**, *435*, 226809; c) S. Kato, S. Yamaguchi, W. Yoshimune, Y. Matsuoka, A. Kato, Y. Nagai, T. Suzuki, *Electrochem. Commun.* **2020**, *111*, 106644; d) S. de Angelis, H. P. Nguyen, S. Nagao, K. Kishita, F. Marone, F. N. Büchi, *Chem.*

Eng. Sci. **2021**, *10*, 100091; e) S. Yamaguchi, S. Kato, A. Kato, Y. Matsuoka, Y. Nagai, T. Suzuki, *Electrochem. Commun.* **2021**, *128*, 107059; f) S. Yamaguchi, S. Kato, W. Yoshimune, D. Setoyama, A. Kato, Y. Nagai, T. Suzuki, A. Takeuchi, K. Uesugi, *J. Synchrotron Radiat.* **2022**, *29*, 1258; g) T. Sugahara, T. Sasabe, H. Naito, M. Kodama, S. Hirai, *ECS Trans.* **2022**, *109*, 135; h) H. Matsui, T. Ohta, T. Nakamura, T. Uruga, M. Tada, *Phys. Chem. Chem. Phys.* ***inpress***. DOI: 10.1039/D4CP00728J

[11] K. Aliyah, C. Prehal, J. S. Diercks, N. Diklić, L. Xu, S. Ünsal, C. Appel, B. R. Pauw, G. J. Smales, M. Guizar-Sicairos, J. Herranz, L. Gubler, F. N. Büchi, J. Eller, *ACS Appl. Mater. Interfaces* **2023**, *15*, 26538.

[12] a) N. Tsuji, Y. Tsuji, Y. Uchimoto, H. Imai, Y. Sakurai, *Appl. Sci.* **2021**, *11*, 3851; b) T. Miyazawa, N, Tsuji, D. Fujioka, T. Kaneko, Y. Mizuno, Y. Uchimoto, H. Imai, Y. Sakurai, *Appl. Sci.* **2023**, *13*, 10753.

[13] K. Kodama, T. Nagai, A. Kuwaki, R. Jinnouchi, Y. Morimoto, *Nat. Nanotechnol.* **2021**, *16*, 140.

[14] W. Yoshimune, S. Yamaguchi, S. Kato, *Energy Fuels* **2023**, *37*, 7424.

[15] a) A. Kusoglu, A. Z. Weber, *Chem. Rev.* **2017**, *117*, 987; b) J. Peron, A. Mani, X. S. Zhao, D. Edwards, M. Adachi, T. Soboleva, Z. Q. Shi, Z. Xie, T. Navessin, S. Holdcroft, *J. Membr. Sci.* **2010**, *356*, 44.

[16] a) X. R. Wang, Y. Ma, J. Gao, T. Li, G. Z. Jiang, Z. Y. Sun, *Int. J. Hydrogen Energy* **2021**, *46*, 12206; b) S. Jang, Y. S. Kang, D. Kim, S. Park, C. Seol, S. Lee, S. M. Kim, S. J. Yoo, *Adv. Mater.* **2023**, *35*, 2204902.

[17] a) S. J. Normile, D. C. Sabarirajan, O. Calzada, V. de Andrade, X. Xiao, P. Mandal, D. Y. Parkinson, A. Serov, P. Atanassov, I. V. Zenyuk, *Mater. Today Energy* **2018**, *9*, 187; b) J. Liu, R. M. Talarposhti, T. Asset, D. C. Sabarirajan, D. Y. Parkinson, P. Atanassov, I. V. Zenyuk, *ACS Appl. Energy Mater.* **2019**, *2*, 3542; c) S. K. Babu, D. Spernjak, R. Mukundan, D. S. Hussey, D. L. Jacobson, H. T. Chung, G. Wu, A. J. Steinbach, S. Litster, R. L. Borup, P. Zelenay, *J. Power Sources* **2020**, *472*, 228442.

[18] a) A. Schneider, C. Wieser, J. Roth, L. Helfen, *J. Power Sources* **2010**, *195*, 6349; b) J. Roth, J. Eller, F. N. Büchi, *J. Electrochem. Soc.* **2012**, *159*, F449; c) D. Kulkarni, S. J. Normile, L. G. Connolly, I. V. Zenyuk, *J. Phys. Energy* **2020**, *2*, 044005.

[19] a) Z. Yu, R. N. Carter, J. Zhang, *Fuel Cells* **2012**, *12*, 557; b) S. Shukla, F. Wei, M. Mandal, J. Zhou, M. S. Saha, J. Stumper, M. Secanell, *J. Electrochem. Soc.* **2019**, *166*, F1142.

[20] R. B. Von Dreele, M. R. Suchomel, B. H. Toby, Advanced photon source – Compute X-ray absorption, https://11bm.xray.aps.anl.gov/absorb/absorb.php, accessed: April, **2024**.

[21] M. Inaba, Y. Kamitaka, K. Kodama, *J. Electroanal. Chem.* **2021**, *886*, 115115.

[22] W. Yoshimune, *Results Chem.* **2023**, *5*, 100738.

[23] A. D. Shum, D. Y. Parkinson, X. Xiao, A. Z. Weber, O. S. Burheim, I. V. Zenyuk, *Electrochim. Acta* **2017**, *256*, 279.

[24] a) I. V. Zenyuk, R. Taspinar, A. R. Kalidindi, E. C. Kumbur, S. Litster, *J. Electrochem. Soc.* **2014**, *161*, F3091; b) I. V. Zenyuk, E.C. Kumbur, S. Litster, *J. Power Sources* **2016**, *241*, 379; c) S. Prass, S. Hasanpour, P. K. Sow, A. B. Phillion, W. Mérida, *J. Power Sources* **2016**, *319*, 82; d) Y. Bao, Z. Wang, Y. Gan, *Energy Technol.* **2022**, *10*, 2201028.

[25] a) K. Shigemasa, H. Sato, Y. Otsuki, M. Kurosu, T. Araki, *Electrochim. Acta* **2021**, *365*, 137383; b) C. Csoklich, M. Sabharwal, T. J. Schmidt, F. N. Büchi, *J. Power Sources* **2022**, *540*, 231539.

[26] a) T. Mashio, K. Sato, A. Ohma, *Electrochim. Acta* **2014**, *140*, 238; b) W. Olbrich, T. Kadyk, U. Sauter, M. Eikerling, *Electrochim. Acta* **2022**, *431*, 140850; c) T. Kaneko, J. Ooyama, M. Ohki, H. Kanesaka, Y. Yoshimoto, I. Kinefuchi, *Int. J. Heat Mass Transfer* **2023**, *200*, 123491.

[27] a) J. Mishler, Y. Wang, R. Lujan, R. Mukundan, R. L. Borup, *J. Electrochem. Soc.* **2013**, *160*, F514; b) A. Pistono, C. A. Rice, *J. Electrochem. Soc.* **2017**, *164*, F582.

[28] W. Yoshimune, M. Harada, *Electrochem. Commun.* **2021**, *130*, 107099.

[29] T. Nonaka, K. Dohmae, Y. Hayashi, T. Araki, S. Yamaguchi, Y. Nagai, Y. Hirose, T. Tanaka, H. Kitamura, T. Uruga, H. Yamazaki, H. Yumoto, H. Ohashi, S. Goto, *AIP Conf. Proc.* **2016**, *1741*, 030043.

The table of contents entry:

Operando synchrotron X-ray radiography reveals the transient liquid water distribution in the Pt loading catalyst layer and gas diffusion layer of a polymer electrolyte fuel cell, representing a new method of assessing the water retention capacity of Pt loading catalyst layers in relation to flooding tolerance and cold-start capability.

W. Yoshimune, A. Kato, T. Hayakawa, S. Yamaguchi, S. Kato*

Liquid Water Visualization in the Pt-Loading Catalyst Layers of Polymer Electrolyte Fuel Cells Using *Operando* Synchrotron X-ray Radiography

ToC figure